

HYPersonic AERODYNAMIC APPRAISAL OF WINGED BLUNT, RATHER SHARP AND SPATULED BODY RE-ENTRY VEHICLES

Antonio Viviani*, Giuseppe Pezzella**

* Second University of Naples, via Roma, Aversa. Italy,

** Italian Aerospace Research Centre, via Maiorise, Capua. Italy

Abstract

The paper deals with the hypersonic aerodynamic analysis of three reusable and unmanned flying laboratories designed to perform a return flight from low Earth orbit to provide experimental data in the framework of re-entry technologies. Several design approaches, ranging from low-order methods to computational fluid dynamics analyses, have been addressed in this work. In particular, vehicles aerodynamic performances for a wide range of free stream flow conditions, including reacting and non-reacting flow and different angles of attack, have been provided and in some cases compared. Computational fluid dynamics results confirm that real gas effects seem to be fundamental for the assessment of the concept aerodynamics, especially concerning pitching moment evaluation.

1 Introduction

This paper deals with the aerodynamic performance analysis of three reusable and unmanned flying laboratories designed to perform an experimental flight return from low Earth orbit. Therefore, each vehicle concept belongs to the class of orbital re-entry vehicle (ORV) e.g., re-entry energy of the order of 25 MJ/kg. Indeed, concepts under investigation in the present research effort are conceived as flying test beds (FTB) that will re-enter the Earth's atmosphere, thus allowing to perform a number of experiments on critical re-entry technologies. For example, the FTB may be useful to demonstrate maneuverability in the upper atmosphere, to test advanced thermo-

structure concepts, such as leading edges made of advanced thermal protection material (TPM), and to investigate the flowfield features during re-entry in order to validate numerical (e.g., CFD) and experimental prediction capabilities.

In particular, the vehicle may provide aerodynamic and aerothermodynamic flight data to correlate with ground test (e.g., the CIRA Plasma Wind Tunnel "Scirocco") results, thus providing new insights into the understanding of complex aerothermodynamic phenomena occurring in flight and improving prediction methodologies and extrapolation to flight capabilities.

Right now Europe has undertaken the development of three very different FTBs, namely ARD (*atmospheric re-entry demonstrator*), Expert (*European experimental reentry testbed*), and IXV (*intermediate experimental vehicle*). ARD was a scaled-down version of an Apollo capsule. It was launched by ARIANE 5 V503 on October 21, 1998. After a fully successful sub-orbital and re-entry flight, it was recovered in the Pacific Ocean [1]. ARD allowed Europe to assess the aerodynamics of such a kind of capsule that still represents a very attractive design solution for what concerns manned high energy re-entry (e.g., return from Mars/Moon missions). Expert, not yet flown, is a small sphere-cone FTB designed to perform several in-flight experiments, such as for example advanced thermal protection system (TPS), wall catalyticity, flow transition assessment and so on [2]. Finally, the Intermediate Experimental Vehicle, which is still under development by the European Space Agency (ESA), is a rather blunt FTB which

features a lifting-body configuration. It will face re-entry flight conditions in the fall 2014 at the end of a sub-orbital flight characterized by an energy level very close to that of an orbital re-entry (e.g., 25 MJ/kg) [3]. IXV will allow to address several in-flight experiments like GN&C of a flapped aeroshape, TPS catalyticity, and etc. The aerodynamic characterization of IXV can be found in [4]. Generally speaking, a reusable ORV operates at different flight regimes from subsonic to hypersonic speeds. A typical mission profile includes: ascent phase, where the spacecraft is attached to a launch vehicle and placed at an altitude; orbit phase, where vehicle orbits in space till completion of desired mission; and descent phase, where the ORV re-enters in atmosphere and lands like a conventional airplane for subsequent use. During the descent up to landing phase the spacecraft encounters subsonic speeds. Therefore, the choice of vehicle aeroshape and its aerodynamic characterization at hypersonic speeds is of vital importance for safe return. Usually, the vehicle configuration is continuously adapted throughout the design phase by means of a multidisciplinary trade-off study involving several concepts. Of course the winning configuration from the aerothermal point of view is the one showing, at the same time, the best aerodynamic and aerothermodynamic performances. Right now the most promising vehicle configurations, resulted from trade-off design analyses, are shown from Figure 1 to Figure 4.

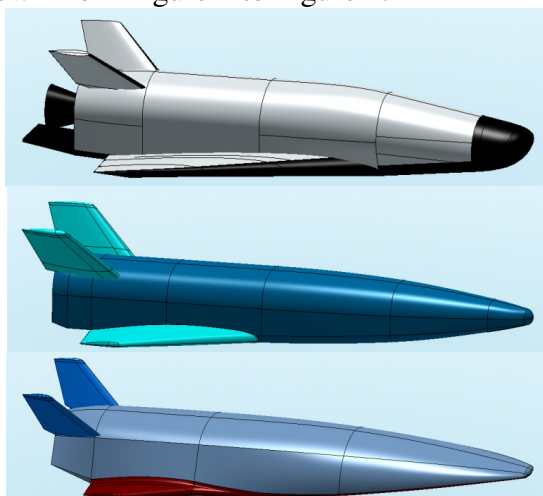


Figure 1 Rather blunt (up), sharp (middle) and spatulated body configurations.

Figure 2 shows the rather sharp vehicle configuration, namely ORV-WBS. In this figure the concept appears also docked with the service module with deployed solar panels (e.g., orbital stationing phase) [5][6].

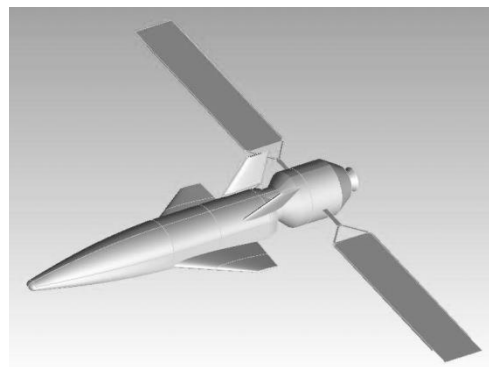


Figure 2 Rather sharp configuration, namely ORV-WBS and the service module with solar panels [5][6].

The rather blunt configuration, named ORV-WBB is provided in Figure 3 [6].

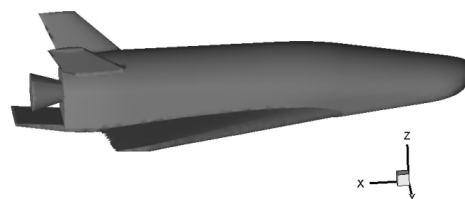


Figure 3 Rather blunt vehicle configuration, named ORV-WBB [6].

Finally, Figure 4 displays a spatulated-body (SB) configuration, namely ORV_SB [6].

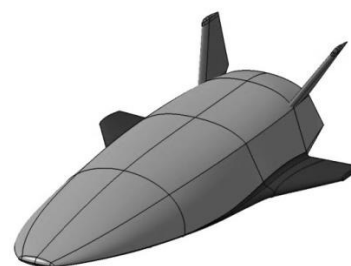


Figure 4. The Spatular body configuration, namely ORV-SB [6].

It is worth to note that ORV concepts show different aeroshapes to address different experimental investigation aims. For example, the ORV-SB configuration is most attractive considering that it represents the only viable way to accomplish and optimize the integration

of scramjet propulsion with the vehicle aerodynamic configuration (see Figure 5, where the ORV-SB features a scramjet engine on the belly side), thus evolving toward waverider aeroshape [7].

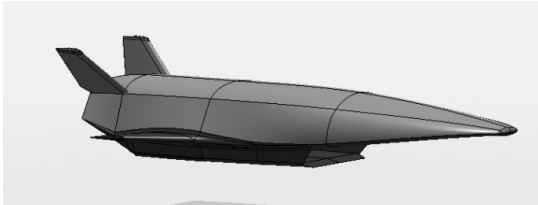


Figure 5. The Spatular body configuration with scramjet engine.

Indeed, since the beginning of aviation, the trend in aircraft design has been towards greater speed. The next frontier of speed envelope is travel at hypersonic speeds. One of the most practical and efficient approach to travel at these high speeds is known as the waverider. Figure 6 shows that concerning high-performance flight vehicle architecture converges with the technology of airbreathing configuration.

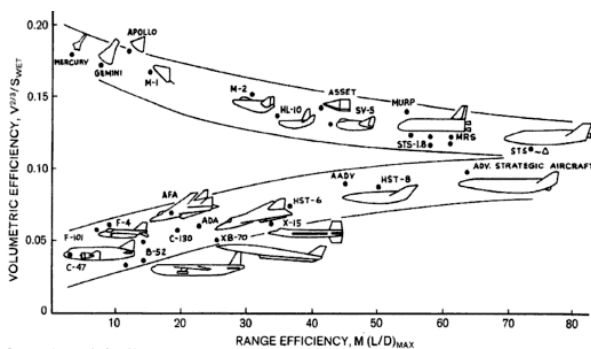


Figure 6 Space and atmospheric vehicle development coverage, so the technology of high-performance launchers converges with the technology of airbreathing aircraft. M=Mach number [7]

Such a configuration demands high aerodynamic efficiency [7]. Indeed, the most efficient hypersonic lifting surface is the infinitely thin flat plate, provided that its lift-to-drag ratio is the highest that can be achieved at hypersonic speeds. The flat plate, however, is obviously not practical, especially since it cannot contain any volume for payload, engines, fuel, etc. Therefore, a more realistic configuration design converges to a spatular vehicle architecture. The characteristics of this aeroshape are: very small frontal area and highly streamlined configuration to minimize

total surface area; very little wing area, but the fuselage is often shaped to generate additional lift; and propulsion assembly highly integrated into the vehicle fuselage.

Anyway, all concepts under investigation belong to the class of the winged body vehicles. Such configurations, however, differ in terms of several vehicle's features as for example planform shape, cross section, nose camber, wing swept angle and, vertical empennages. Differences in concept aeroshapes can be clearly appreciated in Figure 7, where each aeroshape is over imposed on each other.

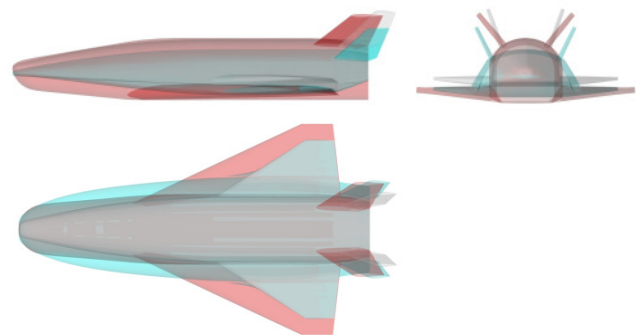


Figure 7 ORV aeroshapes comparison

In this framework, this research effort provides an overview of the aerodynamic performances of these ORVs at hypersonic speed in continuum flow condition. Both low-order methods (i.e., hypersonic panel methods) and CFD design analysis have been considered to assess vehicle aerodynamic characteristics, compliant with a phase-A design level. Low-order methods design approach has been extensively used; while CFD simulations are performed to address the reliability of low-order method design results and to investigate on complex flowfield phenomena not predictable with simplified tools [8],[9],[10]. Indeed, the range between Mach 2 to Mach 25 is analyzed and both perfect and reacting gas CFD simulations are performed at several points of the flight scenario. At flight conditions where real gas effects occur the air is modeled as a mixture of five species in thermo-chemical non-equilibrium conditions. In fact, it is well known that the pitching moment can be highly modified by high temperature effects, thus affecting vehicle's stability behavior and trimming conditions [11]. Finally, an analysis of

the longitudinal and lateral-directional stability has been also provided for one concept, together with some of main interesting features of the flowfield past the vehicles at different Mach numbers.

2 Vehicles Description and Flight Scenario

Vehicle concepts feature a compact wing-body configuration equipped with a rounded edge delta-like fuselage cross section, a delta wing, and V-tail. The vehicle architecture shows a blended wing body interface and a flat bottomed surface to increase its overall hypersonic performance. The fuselage was designed to be longitudinally tapered, in order to improve aerodynamics and lateral-directional stability, and with a cross section large enough to accommodate all the vehicle subsystems. The last fuselage's feature has a large impact on vehicle performance. In fact, from the aerodynamic point of view, the lift and the aerodynamic efficiency are mainly determined by the fuselage fineness and by the shape of the vehicle cross section [12]. The forebody is characterized by a rather simple cone-sphere geometry with smooth streamlined surfaces on the upper and lower side of fuselage, and by the nose drop-down configuration, typical of winged hypersonic vehicles. The nose camber is low enough to reduce elevons size in order to provide desired trim range and to improve internal packaging. The wing size and location were defined on the basis of trade-off studies so to improve vehicle aerodynamics and to provide static stability and controllability during flight [8],[10],[13].

Finally, the wing is swept back to assure best performance with respect to supersonic drag and aerodynamic heating. A properly designed strake could be added in the future, depending on the confirmation of a specific landing requirement. A wing dihedral angle of 5 deg is also provided to enhance vehicle lateral-directional stability. The wing also features a high length-to-width ratio to minimize drag, and a section shape that is maintained from root to wing tip; a leading edge that is rather sharp and a nearly flat bottomed surface to dissipate efficiently the aeroheating. Vertical tails sweep

angle is 45 deg. Control power for vehicle is provided by two wing-mounted elevon surfaces (which must serve as ailerons and elevators), and rudders surface. Used symmetrically elevons are the primary controls for the pitch axis, i.e., pitch control. Roll control is obtained through asymmetrical usage of these elevons.

Rudders help to provide the directional control, i.e., sideslip stability. During entry, when the vehicle is flying at high angles of attack, rudders should be augmented by reaction control system (RCS). Then, the vehicle may be provided by a body flap located at the trailing edge of the fuselage in order to augment pitch control and to shield the nozzle of propulsion subsystem (ORV-WBB only). Indeed, trim capability to relieve elevon loads is obtained by body flap deflection. At hypersonic speeds a surface behind the vehicle CoG balances the nose up pitching moment typical of such kind of configuration at hypersonic speeds.

Finally, the aerodynamic control surfaces are large enough to provide stability without sacrificing too much lift.

In the framework of the Flight Mechanics trade-off analyses several re-entry trajectories have been computed thus defining a vehicle flight envelope. For example, Figure 8 shows a number of re-entry trajectories evaluated supposing that the vehicle heat flux constraint ranges between 1.1 and 2 MW/m²; while the dynamic pressure limit is equal to 12 kPa. The Mach-Reynolds numbers grid in the altitude-velocity map of Figure 8 is also reported in order to characterize vehicle aerodynamics, according to the space-based design approach [14].

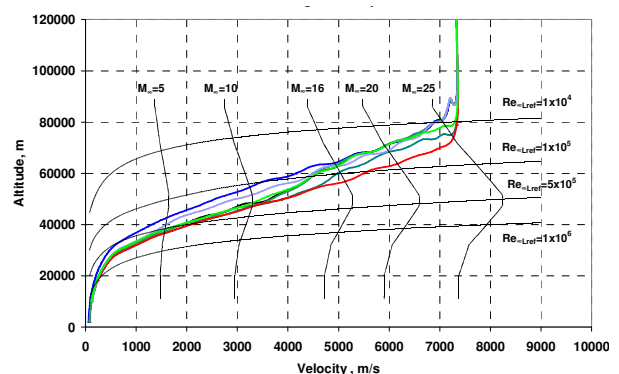


Figure 8. The ORV flight envelope in the velocity-altitude map.

3 Design Approach and Used Tools

A summary overview of the aerodynamic performances of vehicle concepts, compliant with a phase-A design level, is herein performed [13], [14], [15]. The activities goal is to provide concept aerodynamic database (AEDB) for Flight Mechanics and thermal shield design analyses. In fact, it must be verified that vehicle is able to stay within the load constraints (i.e., re-entry corridor) during descent up to conventional runway landing.

The concepts are characterized by a number of extreme loading flight conditions as, for example, transitional flow regime and peak heating conditions. It must return from orbit, fly trimmed throughout hypersonic and supersonic regimes until landing is gained. The AEDB has been provided as a function of Mach number, angle of attack, sideslip angle, aerodynamic control surface deflections, and Reynolds number, according to the Space-Based design approach [14]. This design approach dictates the generation of a complete dataset as function of a number of independent parameters (i.e. M_∞ , Re_∞ , α , β) as schematized in Figure 9.

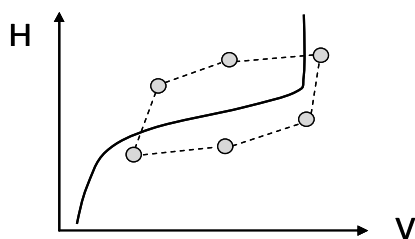


Figure 9 Space-based design approach in the altitude-velocity map.

An accurate aerodynamic analysis of all these flight conditions, however, is very complex and time consuming, and is not compatible with a Phase-A design study, in which fast predicting methods are mandatory. Therefore, the evaluation of the vehicle AEDB was mainly performed by means of engineering tools, while a limited number of more reliable CFD computations (continuum regime only) were performed in order to verify the attained accuracy and to focus on some critical design aspects not predictable with simplified tools [15], [16], [17]. This overall process is referred

to as “anchoring” of the engineering level methods. The anchoring process permits a few, select, CFD solutions to be used beyond the specific flight conditions at which they were original run. Moreover, the anchoring process allows for the cost effective use of high fidelity, and computationally expensive, CFD solutions, early in the design process when the vehicle trajectories are often in a constant state of change [16], [17]. The CFD anchoring “space” is defined by a small number of CFD solutions in Reynolds-Mach-AoA space as shown in Figure 10.

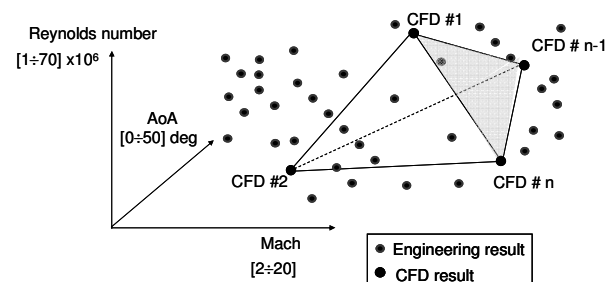


Figure 10 Hypothetical CFD anchoring mesh in Reynolds-Mach-AoA space.

In the framework of low-order methods codes vehicle aerodynamics has been addressed by means of HPM code; while CFD analysis, both Euler and Navier-Stokes, for hypersonic speed have been carried out with commercial code FLUENT.

The HPM code is a 3-D Supersonic-Hypersonic Panel Method code, developed at CIRA, that computes the aerodynamic characteristics of complex arbitrary three-dimensional shapes by using surface inclination methods (SIM) typical of Newtonian aerodynamics [11], [13], [18]. Detailed code description and features can be found in [19], [20], [21].

The CFD code FLUENT solves the full Reynolds Averaged Navier-Stokes equations in a finite volume approach, with a cell centred formulation on a multi-zone block-structured grid. In the present research effort the thermal and chemical non-equilibrium flowfield governing equations are integrated in a density-based approach with an upwind Flux Difference Splitting (FDS) second order upwind numerical scheme for the spatial reconstruction of the

convective terms; while for the diffusive fluxes a cell-centred scheme is applied. In some computations, however, flux vector was computed by using a flux-vector splitting scheme, namely Advection Upstream Splitting Method (AUSM). It provides exact resolution of contact and shock discontinuities and it is less susceptible to Carbuncle phenomena. Implicit solver formulation was considered in the computations of this work. Indeed, due to broader stability characteristics of the implicit formulation, a converged steady-state solution can be obtained much faster using the implicit formulation rather than the explicit one. Global transport properties of the gas mixture relied on semi-empirical rules such as Wilke's mixing rule for viscosity and thermal conductivity. The viscosity and thermal conductivity of i^{th} species was obtained by kinetic theory of gases [11]. For the diffusion coefficient of the i^{th} species in the mixture the multi-component diffusion coefficient was applied, where species mass diffusivity is evaluated by kinetic theory [11]. Flowfield chemical reactions proceed with forward rates that are expressed in the Arrhenius and reaction rate parameters are due to Park [22]. In particular, a number of in-house modifications (i.e., User Defined Functions – UDF–) for the thermal non-equilibrium were considered since vibrational non-equilibrium conditions are not basic code features. In the UFD vibrational relaxation is modeled using a Landau-Teller formulation, where relaxation times are obtained from Millikan and White, assuming simple harmonic oscillators [11]. Finally, the $k-\omega$ SST model has been considered to account for turbulence effects and only steady state computations are carried out so far.

4 Aerodynamic Characterization

Concepts aerodynamic force and moment have been non-dimensionalized by means of the following reference parameters: $L_{\text{ref}}=1.26$ m (wing mean aerodynamic chord–longitudinal reference length); $c_{\text{ref}}=3.60$ m (lateral-directional reference length); $S_{\text{ref}}=5.18$ m² (reference Surface).

4.1 Low order methods aerodynamics

Simplified aerodynamic analysis for supersonic and hypersonic speeds was accomplished on panel mesh close to that shown in Figure 11.

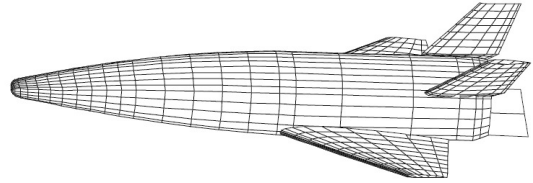


Figure 11 One of the ORV-WSB panel mesh.

In this figure is reported, for example, one of the surface panel mesh considered for the ORV-WSB aerodynamic assessment. Trade-off design analyses highlighted that the best surface inclination methods to consider in assessing vehicle aerodynamic performance are tangent cone and tangent wedge empirical methods for fuselage and wing belly side, respectively; while newtonian method (i.e., $C_p=0$) at vehicle leeside [23],[24]. Some of main results obtained for the ORV-WSB in clean configuration aerodynamic (i.e., no aerodynamic surface deflected) are shown from Figure 12 to Figure 16 .

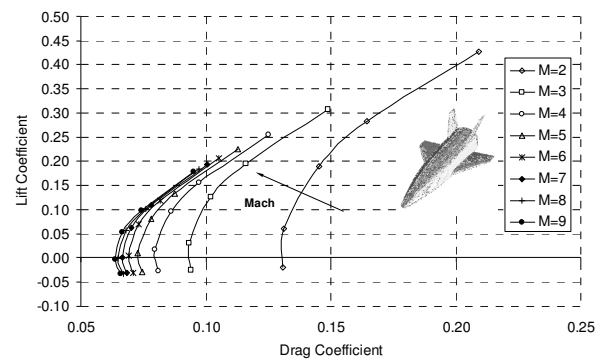


Figure 12 ORV-WSB aerodynamic polars for $2 \leq M_{\infty} \leq 9$

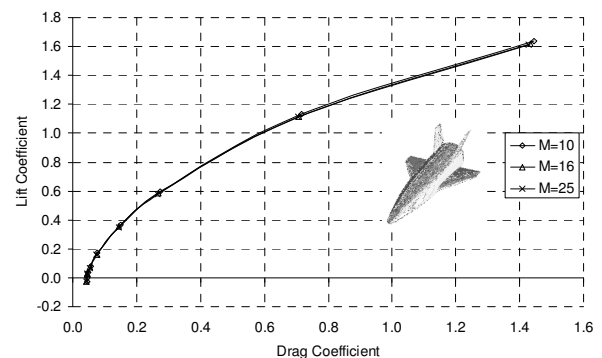


Figure 13 ORV-WSB aerodynamic polars for $10 \leq M_{\infty} \leq 25$

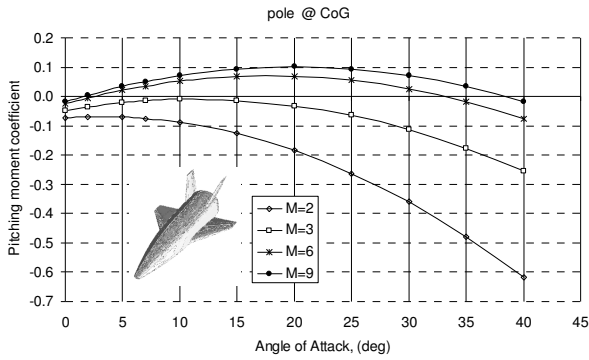


Figure 14 ORV-WSB C_{My} for $2 \leq M_\infty \leq 9$

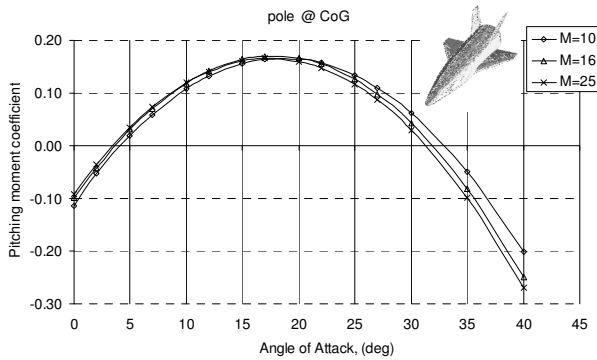


Figure 15 ORV-WSB C_{My} for $10 \leq M_\infty \leq 25$

Figure 14 shows the aerodynamic polars and the pitching moment coefficients for Mach ranging from 2 to 25 and α from 0 to 40 deg. As shown, ORV-WSB drag and lift decrease as Mach number increases up to reach a value that does not change even if Mach still rises, according to the Oswatich principle [11],[13]. Figure 14 also shows that the configuration is statically stable (i.e., $C_{My\alpha} < 0$) for α higher than 20 deg in hypersonic conditions [13]. In particular, the concept in clean configuration features a natural trim point (i.e., $C_{My}=0$) at about 33 to 38 deg AoA for $M_\infty=6$ and 9, respectively. At higher Mach number trim AoA ranges from about 31 to 33 deg. Moreover, the pitching moment behavior highlights that ORV-WSB can be trimmed through flap positive deflection (i.e., downward) only at hypersonic speed. At $M_\infty=2$ and $M_\infty=3$ pitching moment derivative is negative for α larger than 5 deg and 15 deg, respectively. As far as the lateral-directional stability is concerned, Figure 16 shows for $\alpha=5$ deg the effect of sideslip on rolling (CL) and yawing moment (CN) coefficients along with Mach number. Recall that for directional

stability, $CN_\beta > 0$ and for dihedral effect, $CL_\beta < 0$ [13].

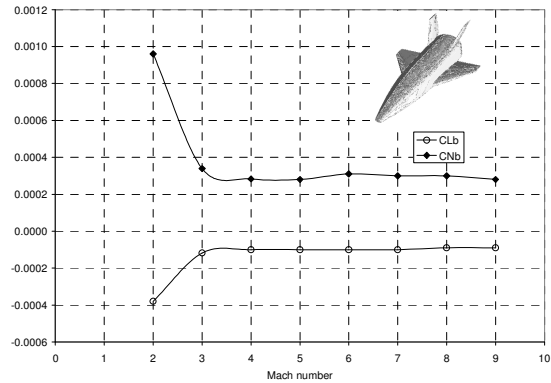


Figure 16 ORV-WSB effect of sideslip on CL_β and CN_β up to $M_\infty=9$, at $\alpha=5$ deg.

As shown, the configuration is statically stable in lateral-directional flight at $\alpha=5$ deg. Note that, the body flap can obviously offer advantages also on both longitudinal and lateral-directional stability by providing margins on CoG location. In fact, the body flap, located on the rear lower portion of the aft fuselage, allows to pitch trim the vehicle while elevons providing concept roll control.

Finally, aerodynamic efficiency and pitching moment comparison at $M_\infty=10$ among ORV-WSB, ORV-WBB, and ORV-SB can be recognized in Figure 17 and Figure 18, respectively.

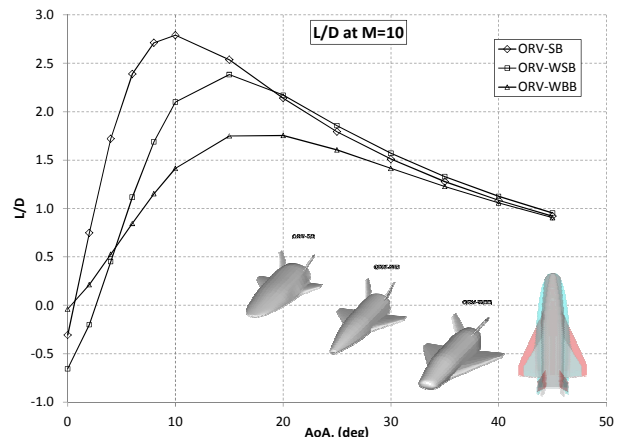


Figure 17. Lift-to-Drag ratio at Mach 10. Comparison among concept performances.

As shown, the ORV-SB concept features the best lift-to-drag ratio up to $\alpha=20$ deg. In particular, the $(L/D)_{max}$ is equal to about 2.8 and is attained at $\alpha=10$ deg AoA. On the other hand,

the maximum aerodynamic efficiency of ORV-WSB and ORV-WBB is reached at about $\alpha=15$ deg and is equal to about 2.4 and 1.8, respectively. For AoA larger than 20 deg differences in aerodynamic efficiency decrease as α increases, and they vanish for $\alpha>35$ deg.

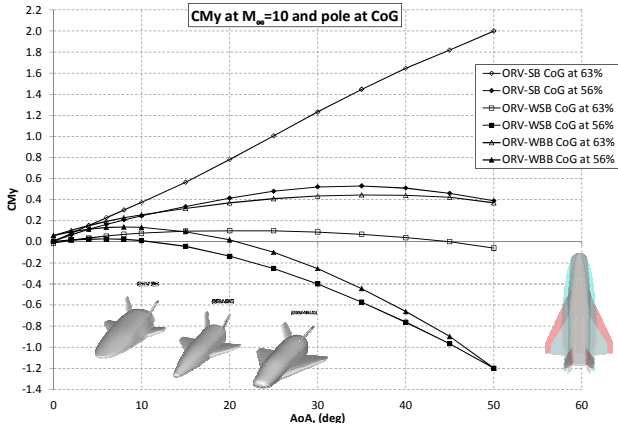


Figure 18. Effect of CoG position on C_{My} at Mach 10. Comparison among concept performances

As a result, in the framework of re-entry at high angle of attack, namely 35-40 deg (e.g., close to that of US Orbiter) differences in aeroshape do not significantly affect the descent flight. In fact, at hypersonic speed and at high AoA vehicle aerodynamic is dictated essentially by its planform shape. In this case, ORV planform shapes are quite close each other (see Figure 7). As far as pitching moment is concerned, the effect of CoG position with respect to the fuselage length on the C_{My} for each vehicle concept is summarized in Figure 18. As shown, when the CoG is at 63% the ORV-SB concept features a strong static instability in longitudinal flight highlighting that the centre of pressure is well ahead of the CoG (i.e., negative static margin); ORV-WBB is static stable in pitch for $\alpha>40$ deg and can be trimmed by positive flap deflections; while ORV-WSB is static stable in longitudinal flight for $\alpha>30$ deg and shows also a natural trim point at about 45 deg AoA. On the contrary for CoG at 56% the ORV-SB concept becomes statically stable in longitudinal flight for $\alpha>35$ deg and trim angles of attack can be attained by positive flap deflections; the other two concepts (WB and WBB) are statically stable in pitch for $\alpha>5$ deg and feature a natural trim point at 10 and 20 deg AoA, respectively. In particular, they can be trimmed at high AoA

by means of negative (i.e., trailing edge up) flap deflections. Anyway, pitching moment behavior versus AoA points out that vehicle subsystems arrangement (i.e., CoG position) must be carefully addressed for a static stable and trimmable vehicle concept.

4.2 CFD-based aerodynamics

For what concerns numerical flowfield computations, on the base of the flight envelope of Figure 8 a number of flight conditions has been chosen to perform some CFD computations in steady state conditions. Numerical results aim to anchor engineering analyses in order to increase them accuracy, and to focus on some critical design aspects not predictable by using simplified tools as, for example, Shock-Shock Interaction (SSI) phenomena on leading edges of both wing and tail, and real gas effects as well [11], [12], [13]. The CFD test matrix is summarized in Table 1.

CFD test matrix										
Mach	AoA @ AoS=0 deg								AoS @ AoA=5 deg	
	0	5	10	20	30	40	45	2	4	8
2	X	X	X	X				X		
3	X	X	X	X				X	X	X
4		X								X
5	X	X	X	X				X		
6	X	X	X	X				X		
7	X	X	X					X		
8		X	X							
8		X	X							
10			X	X	X					
16			X	X	X					
20			X	X	X	X				
20			X	X	X	X				
25					X		X			
X	Perfect Gas									
X	Reacting Gas									

Table 1 CFD test matrix.

Note that each cell identifies a CFD run (i.e., check point). Therefore, the results of forty seven one turbulent CFD computations were performed and some results reported hereinafter. It is worth nothing that, at $M_\infty=8$, 10, 16, 20, and 25 non-equilibrium CFD computations are also carried out. Real gas effects can be important because, during atmospheric re-entry, dissociation process takes place in the shock layer, which can have an influence on the aerodynamic coefficients. Real gas effects are expected to influence stability and control derivatives of vehicle, in particular its pitching moment, as highlighted by first Shuttle re-entry (STS-1) where an unexpected higher nose-up pitching moment required a

HYPERSONIC AERODYNAMIC APPRAISAL OF WINGED BLUNT, RATHER SHARP AND SPATULED BODY RE-ENTRY VEHICLES

body-flap deflection twice than that predicted by the pre-flight analyses to trim the Orbiter [11],[13]. Further, real gas effects cause a shock that lies closer to the vehicle with respect to the position that would characterize a perfect gas case (i.e., thin shock layer) [11],[13]. These effects obviously occur only at high Mach numbers [11], [12], [13]. CFD computations have been carried out on both a multi-block and hybrid unstructured grids similar to those shown in Figure 19 and Figure 20.

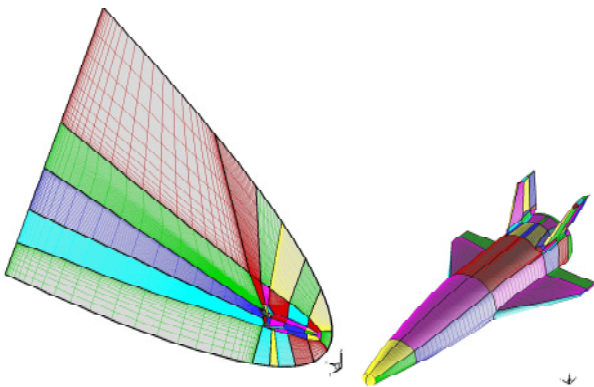


Figure 19. Computational domains. Mesh on symmetry plane and ORV-WSB vehicle.

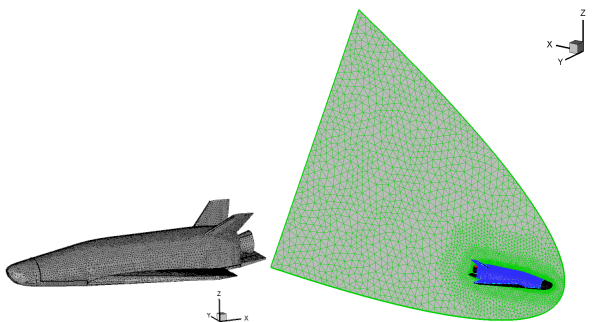


Figure 20. Computational domains. Mesh on vehicle surface and ORV-WBB vehicle.

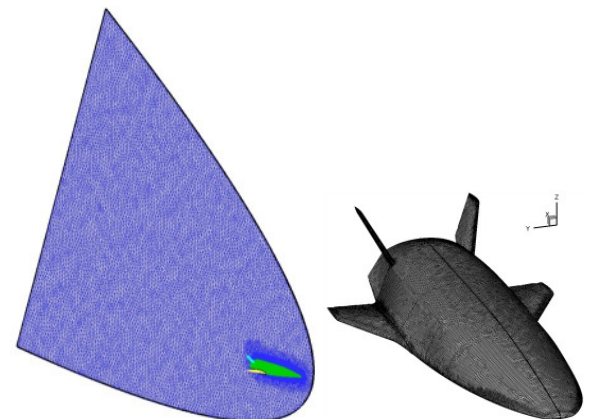


Figure 21. Computational domains. Mesh on vehicle surface and ORV-SB vehicle.

In these figure close-up views of 3-D supersonic mesh on both symmetry plane and vehicle surface can be seen in the case of ORV-WSB (left) and ORV-WBB (right side). Of course, for both computational domains the distribution of surface grid points was dictated by the level of resolution desired in various areas of vehicles such as stagnation region, according to the computational scopes.

Grid refinement in strong gradient regions of flowfield was made through a solution adaptive approach. The coordinate y^+ of the first cell adjacent to the surface is about 1.

As far as numerical results are concerned, it is worth to note that they refer to both converged and grid independent computations [5],[6],[15],[19].

Indeed, aerodynamic results comparison between numerical and engineering analysis in the case of $M_\infty=10, 20$ and for $0<\alpha<40$ deg are provided in Figure 22 and Figure 23.

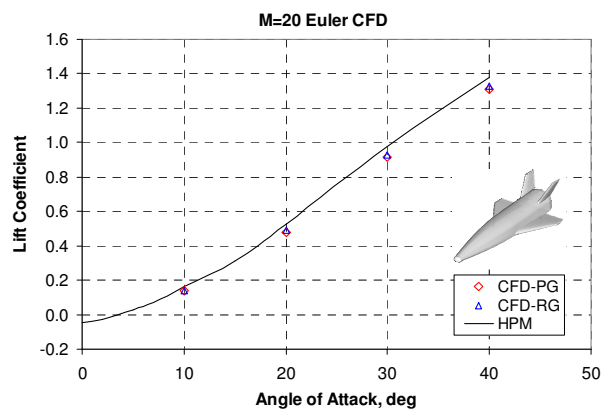
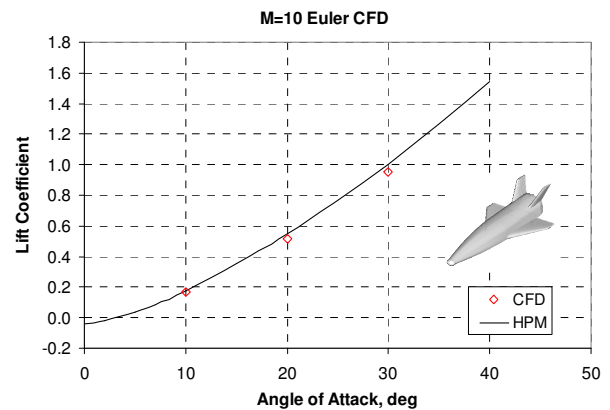


Figure 22. C_L vs α . HPM and CFD results comparison at $M_\infty=10$ and 20. ORV-WSB concept.

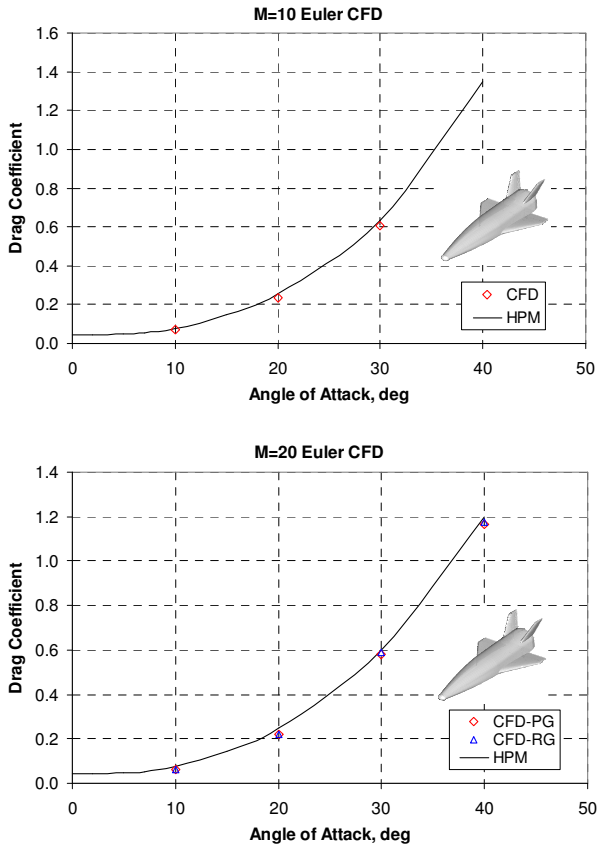


Figure 23. C_D vs α . HPM and CFD results comparison at $M_\infty=10$ and 20. ORV-WSB concept.

As shown, results comparison confirms that engineering-based (i.e., HPM) and numerical data fit each other very well. Moreover, differences between real gas and frozen gas coefficients, collected also in Table 2 for $M_\infty=20$ and $10 < \alpha < 40$ deg, suggest that high temperature gas effects are negligible for lift and drag; whereas a significant effect on vehicle pitching moment is expected along the re-entry trajectory varying from 8 to 50%.

CL			
AoA	PG	RG	Err %
10	0.14	0.14	-1.15
20	0.49	0.48	1.37
30	0.93	0.91	1.97
40	1.33	1.31	1.46

CD			
AoA	PG	RG	Err %
10	0.06	0.06	3.80
20	0.22	0.22	2.00
30	0.59	0.58	1.72
40	1.18	1.16	0.94

CM			
AoA	PG	RG	Err %
10	0.036	0.043	-17.01
20	0.086	0.094	-7.98
30	0.082	0.096	-14.55
40	0.025	0.048	-47.82

Table 2 Real Gas effects on ORV-WSB aerodynamics

Further, in the following figures some of main interesting hypervelocity flowfield features obtained for the ORV-WSB concept are shown. For example, the Mach number and flow species fields for $M_\infty=10$ and 20 at $\alpha=30$, and 40 deg are reported from Figure 24 to Figure 25.

Looking at contour fields on the vehicle symmetry plane, one can appreciate the rather strong bow shock that occurs ahead of the vehicle concepts during descent at these flight conditions, especially at higher AoA. Indeed, Figure 24 shows the Mach number field past the rather sharp wing body vehicle for $M_\infty=10$ and 30 deg AoA [25]. As shown, even if the CFD computations are carried out in the case of perfect gas flow, the bow shock is very close to the vehicle due to its streamlined configuration

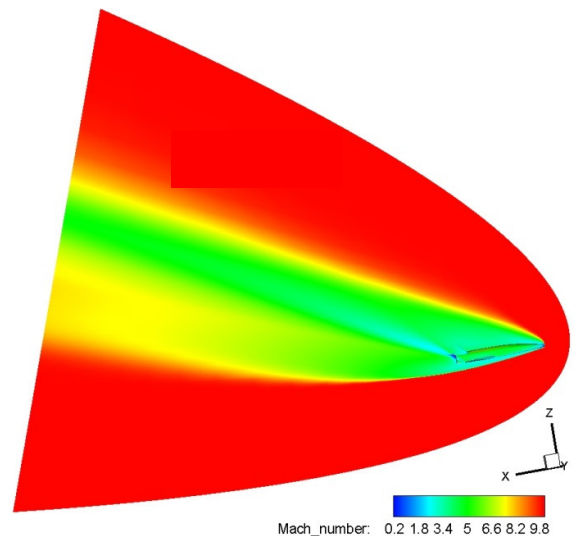


Figure 24. Mach contours on symmetry plane and ORV-WSB surface at $M_\infty=10$ and $\alpha=30$ deg.

In the reacting gas computations air was considered made up of five chemical species (O_2 , N_2 , O , N and NO) and in thermo-chemical non-equilibrium conditions.

For example, the Oxygen (O) mass fractions contour fields at $H_\infty=70$ km, $M_\infty=20$ and $\alpha=40$ deg are shown in Figure 25.

As far as numerical results for the ORV-WBB concept are concerned, Figure 26 to Figure 28 show several flowfield features for the rather blunt vehicle at $M_\infty=25$ and $\alpha=30$ deg.

HYPERSONIC AERODYNAMIC APPRAISAL OF WINGED BLUNT, RATHER SHARP AND SPATULED BODY RE-ENTRY VEHICLES

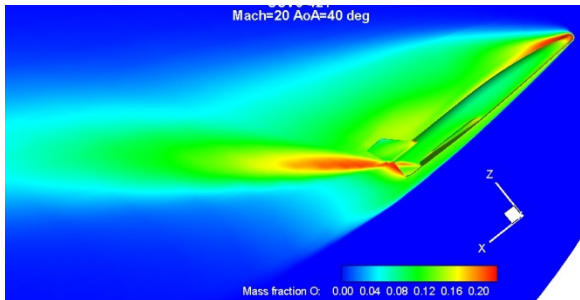


Figure 25. Oxygen mass fractions. CFD computation at $H_{\infty}=70$ km, $M_{\infty}=20$ and $\alpha=40$ deg. ORV-WSB concept.

In particular, Figure 26 and Figure 27 highlight the Mach number and the N_2 mass fraction contour fields on the vehicle symmetry plane and C_p on the concept outer surface, respectively.

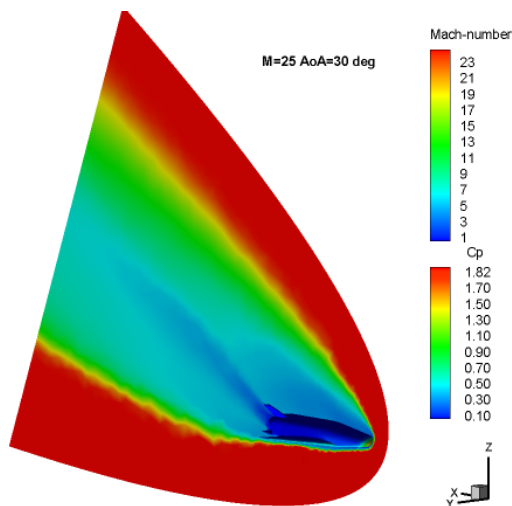


Figure 26. Mach contours on symmetry plane and C_p on ORV-WBB surface at $M_{\infty}=25$ and $\alpha=30$ deg..

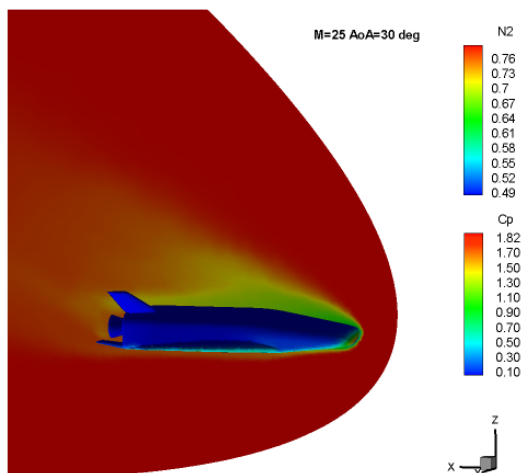


Figure 27. N_2 contours on symmetry plane and C_p on ORV-WBB surface at $M_{\infty}=25$ and $\alpha=30$ deg.

Side and bottom views of the surface distribution of C_p at these flight conditions are summarized in Figure 28.

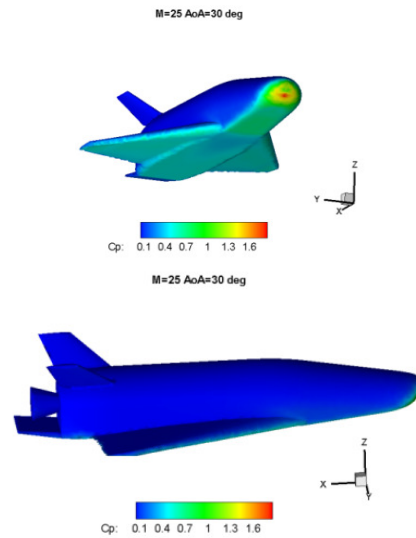


Figure 28. C_p on ORV-WBB surface at $M_{\infty}=25$ and $\alpha=30$ deg.

Hence, in order to get an idea of the bow shock that envelopes the ORV-WBB at $M_{\infty}=25$ and $\alpha=30$ deg, Figure 29 provides three flowfield cross sections where Mach contours are reported.

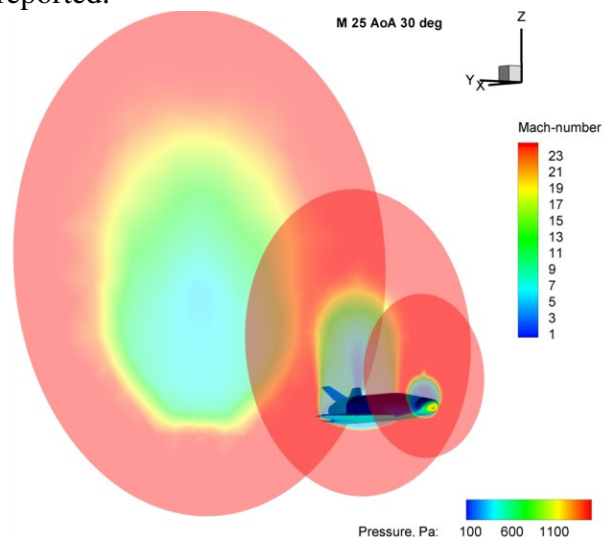


Figure 29. C_p on ORV-WBB surface at $M_{\infty}=25$ and $\alpha=30$ deg. Mach number contours on three flowfield cross sections

For what concerns the flowfield past the ORV-SB concept, Figure 30 shows the Mach number contour field on vehicle symmetry plane and pressure distribution on concept surface at $M_{\infty}=25$ and $\alpha=30$ deg. Streamlines are also provided.

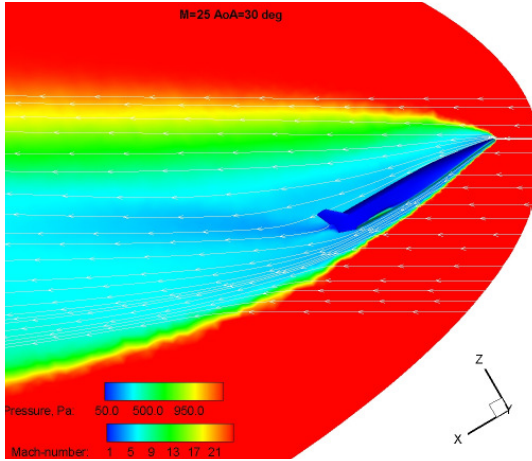


Figure 30. Pressure on ORV-SB surface and Mach number contours on symmetry plane at $M_\infty=25$ and $\alpha=30$ deg.

3-D streamtraces at these flight conditions together with a cross flow section coloured by Mach number are provided in Figure 31. Also in this case a very narrow shock layer is expected for this concept.

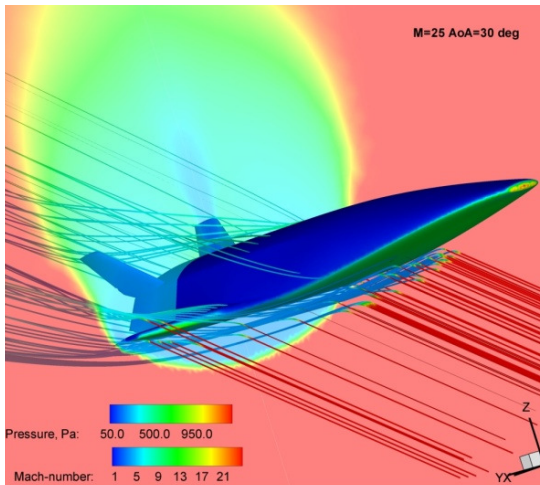


Figure 31. Pressure on ORV-SB surface at $M_\infty=25$ and $\alpha=30$ deg with 3-D streamtraces and flowfield cross section coloured by Mach number.

Finally, results comparison between numerical and engineering-based aerodynamic for ORV-WBB and ORV-SB are summarized in Figure 32 and Figure 33, respectively.

For instance, Figure 32 compares aerodynamic results for axial force coefficient (C_A) and pitching moment coefficient (C_{My}) at $M_\infty=25$ and $\alpha=30$ deg; while Figure 33 provides result comparison for normal force coefficient (C_N) at $M_\infty=10$ and $\alpha=30$ deg and for axial force coefficient at $M_\infty=25$ and $\alpha=30$ and 45 deg.

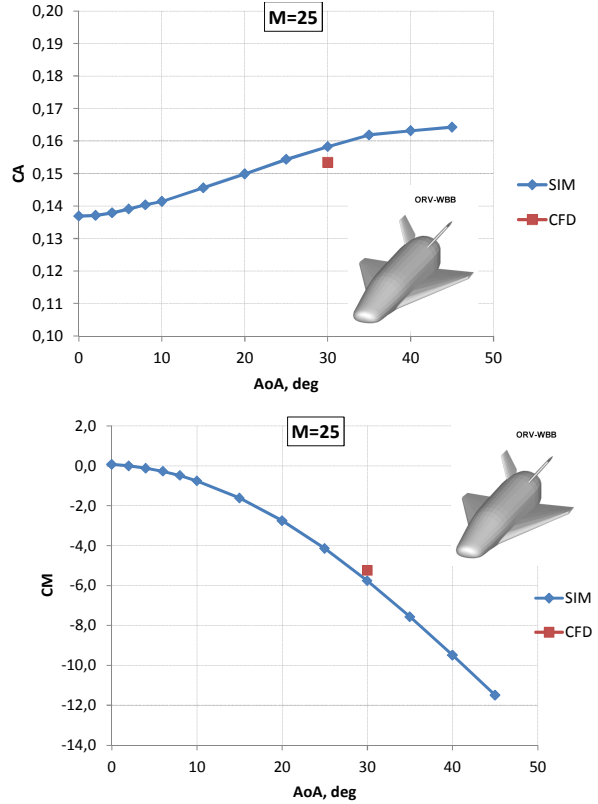


Figure 32. C_A and C_M at $M_\infty=25$ and $\alpha=30$ deg. ORV-WBB concept. CFD and HPM comparison.

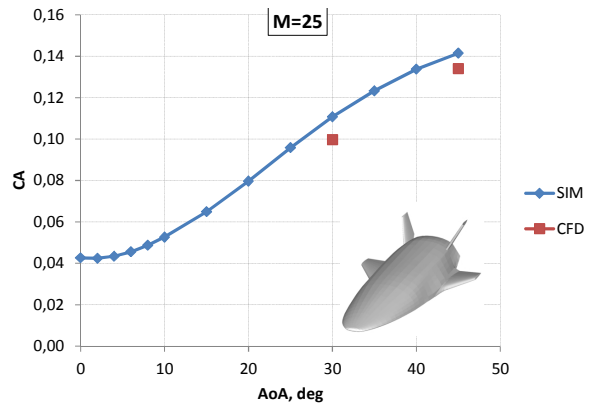
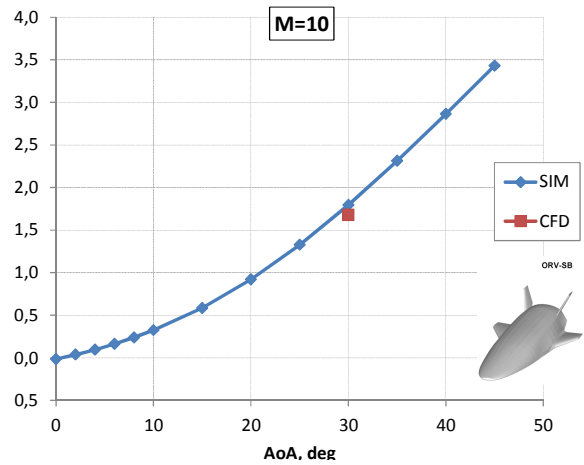


Figure 33. C_A and C_N at $M_\infty=25$ and $\alpha=30$ deg. ORV-SB concept. CFD and HPM comparison.

As shown, also in those cases it is confirmed that HPM provides reliable results in the framework of a phase-A design level.

5 Concluding Remarks

This paper provides a summary overview of aerodynamic performances of three winged vehicle concepts allowing to perform a number of experiments on critical re-entry technologies. Therefore, a possible re-entry mission scenario has been provided and considered for the appraisal of the concepts flight performance. Results of forty seven fully three-dimensional CFD computations of the flowfield past the flying test beds have been presented for the whole continuum flight regime. An assessment of the vehicle aerodynamics performed through low-order method design approach like hypersonic panel methods are shown as well.

Real gas effects on the vehicles aerodynamics have been discussed. Results show that these effects for the ORV-WSB concept flying at $M_\infty=20$ and for α ranging from 10 to 40 deg seem to be negligible for lift and drag due to the rather high streamlined vehicle configuration. So real gas effect are expected to not affect concept re-entry trajectory; while a significant effect on vehicle pitching moment is expected during descent varying from 8 to 50%.

Finally, aerodynamic analysis provided in this work are considered applicable for the prosecution of the trade-off design analysis of the most promising aeroshape to choose for the flying test bed.

References

- [1] Ph. Tran, J.C. Paulat, and P. Boukhobza, "Re-entry Flight Experiments Lessons Learned –The Atmospheric Reentry Demonstrator ARD". RTO-EN-AVT-130.
- [2] A. Schettino, R. Votta, P. Roncioni, M. Di Clemente, M. Gerritsma, C. Chiarelli, D. Ferrarella, "Aerodynamic and Aerothermodynamic Data Base of Expert Capsule" *Proceedings of the West-East High Speed Flow Field Conference*; 19-22 Nov 2007, Moscow, Russia.
- [3] S. Paris, D. Charbonnier, D. Tran, "Experimental and Numerical Investigation of Aerothermal Characteristics of the IXV Hypersonic Vehicle. *Proceeding of the 7th European Symposium on Aerothermodynamics for Space Vehicles*. Brugge, May 9 - 12, 2011.
- [4] G. Pezzella, G. Marino, G. Rufolo, "Aerodynamic Database Development of the ESA Intermediate Experimental Vehicle". *Acta Astronautica*, DOI: 10.1016/j.actaastro.2013.07.019. Vol. 94. Issue 1. January–February 2014. ISSN (0094-5765): pag.(57–72).
- [5] A. Viviani, G. Pezzella, "Aerodynamic Performance Analysis of an Unmanned Re-Entry Vehicle from Hypersonic down to Subsonic Regime". *Proceedings of the 63rd International Astronautical Congress*, Naples, Italy. IAC-12-D2.3.4. 2012.
- [6] A. Viviani, G. Pezzella, "Aerodynamic Performance Analysis of Three Different Vehicle Concepts at Hypersonic Speed", *Proceedings of the XXII Conference of Italian Association of Aeronautics and Astronautics*, 9-12 September 2013. Naples, Italy. Paper 74.
- [7] "Aerodynamic Problems of Hypersonic Vehicles", AGARD Lecture Series No. 42; AGARD-LS-42. Vol.1.
- [8] A. Schettino, G. Pezzella, et al., "Mission Trade-off Analysis of the Italian USV Reentry Flying Test Bed", *Proceedings of the 14th AIAA-AHI Space Planes and Hypersonic Systems and Technologies Conference*; 6-9 Nov 2006, Canberra, (Australia); paper AIAA-2006-8017.
- [9] A. Schettino, G. Pezzella, et al., "Aero-thermal Trade-off Analysis of the Italian USV Re-entry Flying Test Bed", *Proceedings of the 14th AIAA-AHI Space Planes and Hypersonic Systems and Technologies Conference*; 6-9 Nov 2006, Canberra, (Australia); paper AIAA-2006-8114.
- [10] G. Pezzella, F. Battista, A. Schettino, et al., "Hypersonic Aerothermal Environment Preliminary Definition of the CIRA FTB-X Reentry Vehicle", *Proceedings of the West-East High Speed Flow Field Conference*; 19-22 Nov 2007, Moscow, Russia.
- [11] J. D. Anderson, *Hypersonic and High Temperature Gas Dynamics*, McGraw-Hill Book Company, New York, 1989.
- [12] G. Pezzella, M. Marini, P. Roncioni, J. Kauffmann, C. Tomatis. Preliminary Design of Vertical Takeoff Hopper Concept of Future Launchers Preparatory Program. *Journal of Spacecraft and Rockets* 2009. ISSN 0022-4650 vol.46 no.4 (788-799) doi: 10.2514/1.39193.
- [13] J. J. Bertin, *Hypersonic Aerothermodynamics*, AIAA Education Series.
- [14] D.K. Prabhu, System design constraints – Trajectory aerothermal environments, in: RTO AVT/VKI Lecture Series in Critical Technologies for Hypersonic Vehicle Development, May 10–14, 2004.
- [15] G. Pezzella R. Gardi G. Guidotti, C. Richiello, "Aerodynamic and Aerothermodynamic Trade-off Analysis of the Italian USV2 Flying Test Bed in the Framework of an Hypersonic Flight Test".

- Proceeding of 3rd International ARA Days*. 2-4 May 2011. Arcachon. France. AA-1-2011-54.
- [16] D.J. Kinney “Aero-thermodynamics for conceptual design”, *Proceedings of the 42nd AIAA Aerospace Sciences Meeting and Exhibit*, Reno, NV, USA, January 5–8, 2004, AIAA-2004-31.
- [17] D.J. Kinney, “Aerodynamic shape optimization of hypersonic vehicles”, *Proceedings of the 44th AIAA Aerospace Sciences Meeting and Exhibit*, Reno, NV, USA, January 9–12, 2006, AIAA-2006-239.
- [18] E. Bonner, W. Clever, K. Dunn, “Aerodynamic Preliminary Analysis System II Part I- Theory”, NASA Contractor Report 182076. April 1991.
- [19] G. Pezzella, “Aerodynamic and Aerothermodynamic Trade-off Analysis of a Small Hypersonic Flying Test Bed”. *Acta Astronautica*. Vol. 69 Issue 3-4. pp. 209-222. ISSN (0094-5765) doi:10.1016/j.actaastro.2011.03.004. (2011).
- [20] G. Pezzella, “Aerodynamic and Aerothermodynamic design of Future Launchers Preparatory Program Concepts”. *Aerospace Science and Technology*, Vol. 23, Issue 1, pp 233–249. <http://dx.doi.org/10.1016/j.ast.2011.07.011>. (2012).
- [21] G. Pezzella, “Hypersonic Aerothermal Environment Assessment of the CIRA FTB-X Reentry Vehicle”. *Aerospace Science and Technology*, Vol. 25, Issue 1, pp. 190–202. <http://dx.doi.org/10.1016/j.ast.2012.01.007>. (2013).
- [22] C. Park, “Review of Chemical Kinetic Problems of Future NASA Missions: Earth Entries”. *Journal of Thermophysics and Heat Transfer*, Vol. 7. No 3. 1993.
- [23] M. Maughmer, L. Ozoroski, D. Straussfogel, L. Long, “Validation of engineering methods for predicting hypersonic vehicle control forces and moments”, *AIAA Journal of Guidance, Control, and Dynamics* 16 (4) (July–August 1993).
- [24] M. Moore, J. Williams, “Aerodynamic prediction rationale for analyses of hypersonic configurations”, *Proceedings of the 27th Aerospace Sciences Meeting*, Reno, NV, USA, January 9–12, 1989, AIAA-89-0525.
- [25] G. Pezzella, E. Filippone, and M. Serpico, “Re-entry Aerodynamics and Aerothermodynamics Analyses of the Flying Test Bed USV-X in the Framework of a High Lift Return”, *Proceeding of 16th AIAA/DLR/DGLR International Space Planes and Hypersonic Systems and Technologies Conference*, AIAA 2009-7425, 2009.

it as part of their paper. The authors confirm that they give permission, or have obtained permission from the copyright holder of this paper, for the publication and distribution of this paper as part of the ICAS 2014 proceedings or as individual off-prints from the proceedings.

Copyright Statement

The authors confirm that they, and/or their company or organization, hold copyright on all of the original material included in this paper. The authors also confirm that they have obtained permission, from the copyright holder of any third party material included in this paper, to publish